Identification of a Potential Geothermal Resource in Colombia through the Application of Geoelectric Methods at the *Aguas de Vichy* Spring in the Municipality of San Andrés, Santander

Juan C. Mejía-Fragoso
Corresponding author
Universidad Industrial de Santander
camilomejia.geo@gmail.com

José D. Sanabria-Gómez
Universidad Industrial de Santander
jsanabri@uis.edu.co

Rocío Bernal-Olaya
Universidad Industrial de Santander
rbernalo@uis.edu.co

August 13, 2024

Abstract

The *Aguas de Vichy* thermal spring (SAN-001), identified by the Colombian Geological Service (SGC) and located in Santander, Colombia, represents a significant yet underexplored geothermal resource. This study is the first to conduct subsurface imaging of the geothermal system, employing Electrical Resistivity Tomography (ERT) and Induced Polarization (IP) methods to investigate the hydrogeological framework. Geochemical analyses of the spring water indicate high salinity and elevated temperatures, suggesting a substantial energy capacity. The geological setting is characterized by north-south (N-S) and northeast-southwest (NE-SW) faults, intersecting Cretaceous and Precambrian formations, along with a Quaternary aquifer.

Three ERT transects were conducted around the inferred fault, which was hypothesized to be the main conduit for geothermal fluids. Two transects crossing the fault revealed electric resistivity values ranging from near zero to over 1500 $\Omega \cdot$ m, suggesting the presence of zones of clay, groundwater accumulation, and geothermal fluids. High resistivity anomalies at depths of 5 to 10 meters indicate the lower boundaries of the Quaternary deposits. The third transect, located within the Quaternary deposit but far from the fault, exhibited elevated baseline resistivities and a diminished prevalence of low resistivity anomalies, indicating a possible clay deposit with reduced influence

of water. IP measurements validated the presence of geothermal fluids and illuminated areas with elevated chargeability, suggesting the presence of clay levels within the aquifer.

Our findings support the existence of a geothermal system in which convection plays an important role, along with notable advective movements within the aquifer. This suggests a complex interaction of subsurface fluid dynamics, integrating both fault-mediated fluid transport and advection processes rather than being solely advection-dominated as suggested initially. The complexity observed in these findings underscores the need for more detailed studies to enhance our understanding of the dynamics and potential of the geothermal system, which could make a valuable contribution to Colombia's goals for energy sustainability.

***K*eywords** Geothermal · Colombia · Santander · Geophysics · Resistivity

1 Introduction

The tectonic and geological characteristics of Colombia, including its position on the Pacific Ring of Fire and its geodynamic context of convergent plate margins, facilitate surface manifestations of subsurface heat such as volcanoes, thermal springs, and fumaroles. These features represent significant development opportunities, not only for electricity generation but also for the direct utilization of thermal energy [Alfaro et al., 2020].

Geothermal exploration in Colombia began in 1968 with an assessment by Ente nazionale per l'energia elettrica (ENEL), initiated by the Caldas Hydroelectric Power Plant, focusing on the Nevado del Ruiz volcanic complex [Bona and Coviello, 2016]. Though initial efforts paused, exploration resumed in 1983 with a pre-feasibility study by CHEC and expanded significantly in 1997 when the Colombian Geological Service (formerly INGEOMINAS) and companies like ISAGEN started exploring various volcanic regions including Tufiño - Chiles - Cerro Negro, in partnership with Ecuador [Mejía et al., 2014], [Salazar et al., 2017].

Initial estimates of Colombia's hydrothermal geothermal resource potential ranged between 700 and 1370 MWe [Gawell et al., 1999]. This capacity was expected to increase to 1340 - 2210 MWe with advances in drilling and permeability enhancement techniques. By 2020, the Servicio Geológico Colombiano (SGC) estimated the geothermal potential from key convective sources like hot springs and volcanoes at approximately 1170 MWe, suggesting that geothermal energy could meet 20% of Colombia's energy demand [Alfaro et al., 2020].

Despite this potential, many of the critical geothermal zones in Colombia remain underexplored or only in the prefeasibility phase. The Santander department has been recognized by the SGC as having a significant unexplored geothermal potential of 210 kWe. Among these, the *Aguas de Vichy* hot springs in the municipality of San Andrés are highlighted as a geothermal prospect. Geochemical analyses suggest the underlying geothermal reservoir could reach temperatures of 100 °C with high salinity and an expected electricity generation capacity of 80 kWe [Alfaro et al., 2020]. Despite these promising indicators, there remains a lack of comprehensive subsurface data and studies.

Currently, Parex Resources, the Ministry of Mines and Energy, and the Universidad Nacional, Medellín, have launched the first geothermal energy generation project in the Maracas field in Casanare. This facility, which benefits from the coproduction of high temperature water during oil extraction, has an installed capacity of 100 kWe, equivalent to the consumption of approximately 350 homes, capable of

generating up to 72,000 kWh/month and reducing CO_2 emissions by approximately 550 tons per year [Márquez et al., 2021].

In addition to the above mentioned, Parex has another pilot in Campo La Rumba (low enthalpy), in the municipality of Aguazul in Casanare, with a capacity of 35 kW and generation of 672 kWh/day, equivalent to the consumption of 117 homes. Ecopetrol is developing another pilot in Chichimene (also low enthalpy), in Acacías, Meta, with a capacity of 2 MW and a generation of 38,400 kWh/day, equivalent to the consumption of 6,659 households [Jorquera, 2021]. Today, Parex Resources has not yet begun the first formal geothermal energy project in the northeast of the country, with the authorization of the National Government.

Geothermal systems are primarily categorized by enthalpy levels—high, medium, and low—with high-enthalpy systems typically used for electric power generation and medium to low-enthalpy systems for thermal energy [Pesce and Miranda, 2003]. Some low enthalpy systems are also suitable for electricity generation using binary cycle technology [Chandrasekharam and Bundschuh, 2008]. These systems are also classified as either convection-dominated, where heat is transported via fluid movement through permeable structures, or conduction-dominated, which do not rely on fluid movement and are associated with gradual temperature increases with depth [(IGA), 2014].

Local examples of conduction-dominated systems include the Parex Resources pilot project in Casanare's Las Maracas and Rumba fields, which is undergoing evaluations to enhance conduction-dominated and low-entalphy geothermal resources in the Llanos Basin [López-Ramos et al., 2022]. Similar studies are underway internationally, such as in China, where the feasibility of using abandoned oil and gas wells for energy is being assessed [Bu et al., 2012], and in Uruguay, where the geothermal potential of sedimentary onshore basins is explored [Morales et al., 2021].

Convection-dominated systems are more extensively studied as they are associated with volcanoes, fumaroles, hot springs, etc. In Colombia, most geothermal prospects are convective [Alfaro et al., 2020], with the geothermal system of the Nevado del Ruiz volcano being the most studied area [Bona and Coviello, 2016]. The geothermal area of Paipa has also been significantly investigated, including resistive models [González-Idárraga, 2020]; the Azufral volcano, on the other hand, was considered a high-priority geothermal area [Ovalle, 2020].

Convection-dominated geothermal systems have various global analogs that have been the focus of numerous geophysical studies aiming to model the geothermal system and infer its associated mechanisms; one example is the Hammam Sayala hot springs, where Vertical Electrical Soundings were conducted and a 2D model was developed using Electrical Resistivity Tomography to define the geothermal model of these waters [Chabaane et al., 2017].

Similarly, an integrated study using various geophysical methods (Surface Temperature, Magnetotellurics, Microtremor, and radon measurements) was conducted to map a geothermal reservoir associated with a convective system in Langfang, China; aiming to determine the range of the geothermal anomaly, explore the characteristics of the geothermal fluid and the associated fault, and identify the lithology and its depth, to ultimately propose a geothermal model where the fluid infiltrates deep, heats in basement rocks, and then rises through the fault [Tian et al., 2022].

In Iceland, a study was conducted in the Krafla geothermal area [Arnason et al., 2000] using resistivity and magnetotelluric data to identify high-conductivity zones associated with the presence of geothermal fluids. Similarly, resistive methods have been used in the exploration of geothermal systems in Mexico, such as in the geothermal areas of Los Humeros and Acoculco [Romo-Jones et al., 2021] where ERT and MT data were used to identify zones of low resistivity associated with geothermal fluids and geological structures. Magnetotelluric resistivity and seismic data were used in the Wairakei-Tauhara

geothermal field (New Zealand) to identify zones of high electrical conductivity associated with the presence of geothermal fluids and geological structures [Hunt et al., 2009].

Resistive methods, such as electrical resistivity tomography (ERT) and vertical electrical sounding (VES), have been used in the exploration of groundwater and geothermal systems since the mid-20th century [Zohdy et al., 1974]. These methods are based on the measurement of the electrical resistivity of the subsurface, which is sensitive to the presence of fluids, geological structures, and temperature changes; thus allowing their detection [Dentith and Mudge, 2014]. In the exploration of convective geothermal deposits, the resistive method is used to identify the recharge and discharge zones of geothermal fluids, as well as to determine the geometry of the fracture system that controls the movement of fluids. The results of the resistive method are combined with information from other geophysical techniques to obtain a complete image of the geothermal deposit [Kana et al., 2015].

Similarly, advanced techniques for modeling and processing resistive data have been developed that have improved the resolution and accuracy of these methods. These improvements include the use of 3D inversions [Spichak and Manzella, 2009] and joint modeling techniques with other geophysical methods, such as magnetotellurics (MT) and seismic. In addition, special attention has been paid to the modeling of convective geothermal systems, where the interaction between fluids and geological structures is key to the formation of geothermal resources.

In the present study, we show the first subsurface imaging of the *Aguas de Vichy* hot springs, utilizing geoelectrical methods to explore this previously unexplored geothermal resource. These methods are particularly effective for investigating geothermal systems dominated by fluid circulation. Our research aims to delineate the behavior and distribution of geothermal fluids at the surface, verify the hypothesis that the geothermal system is predominantly advection-dominated [Alfaro, 2017], and propose a new hypothesis suggesting the presence of a thermal water plume associated with an inferred major fault, which would indicate a potential convection-dominated geothermal system instead. Understanding these dynamics could significantly enhance our knowledge of Santander's geothermal capabilities and contribute to achieving Colombia's energy sustainability objectives.

2 *Aguas de Vichy* Thermal Springs

The municipal seat of San Andrés is situated at 6°49'N latitude and 72°51'W longitude from the Greenwich meridian, at an altitude of 1,617 meters above sea level. The region has an average temperature of 19°C and is located 104 kilometers away from Bucaramanga. The municipality covers an area of 278 km^2. Within the municipality, a thermal spring emerges along the banks of the Guaca River, three kilometers south of the town center via the road to Molagavita and Málaga. To reach the spring, one must walk approximately 500 meters west from the road to the river channel. This thermal spring is named *Aguas de Vichy* [Alfaro and Ortiz, 2011].

The area is notably affected by intense faulting and folding, predominantly oriented N-S and NE-SW. A covered fault at the spring emergence point, mapped with a NNW-SSE orientation, juxtaposes Paleozoic units with Cretaceous units [Ward et al., 1977] (Figure 1). Another structural feature, the Baraya fault, is located two kilometers east of the spring. This N-S trending normal fault with right-lateral movement juxtaposes sedimentary rocks from the Paleozoic, Jurassic, and Cretaceous periods.

The geological units outcropping range from the Ordovician (pre-Devonian) to the Quaternary. Generally, there are intrusive igneous rocks from the Jurassic (Santa Barbara quartz monzonite) that intrude older metamorphic rocks such as the Bucaramanga Gneiss and the Silgará Formation, which constitute the crystalline basement of the area. Above the basement, a series of sedimentary units

are deposited, ranging from the Devonian to the Quaternary, along with a series of recent deposits that continue to accumulate to the present. These sequences have different contact relationships with each other and are also affected by significant structural control, evidence of the complex geological history of the territory.

The thermal waters in San Andrés are classified as sodium chloride type, enriched with notable levels of bicarbonates and calcium (Table 1). Taking into account the elevated levels of total dissolved solids and the specific ionic composition, it is hypothesized that these waters are significantly influenced by deep infiltration from a saline source [Alfaro and Ortiz, 2011], dominated by an advective (lateral) flow [Alfaro, 2017].

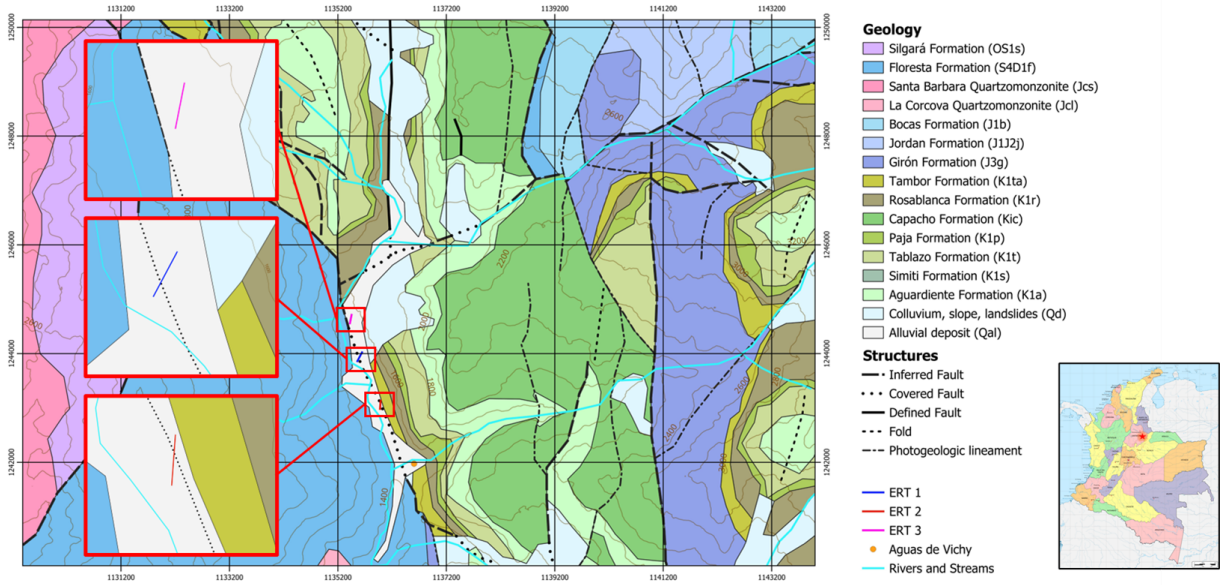

Figure 1: Location of the *Aguas de Vichy* thermal springs, geological map and location of the ERT surveys. Modified from [Ward et al., 1977] and [Alfaro and Ortiz, 2011].

Thermal springs emerge at the southern corner of a quaternary alluvial deposit, which overlays an inferred covered fault and is influenced by the Guaca River and the Lizagura Stream. This deposit forms part of a larger, unconfined aquifer system with regional extent, composed of non-consolidated quaternary sediments and partially consolidated tertiary rocks (Jurassic and Cretaceous) within a fluvial environment. Locally, parts of the aquifer system may be confined and typically exhibit moderate productivity [Ríos et al., 2002].

The quaternary deposit was classified as an alluvial deposit [Alfaro and Ortiz, 2011], though it has not been extensively studied further. Alluvial deposits are typically found in ravines, streams, and broad topographic surfaces, often forming well-developed terraces, particularly along the margins of river valleys. They result from the transport and deposition of material by water. These deposits are composed of clays, sands, granules, pebbles, cobbles, and blocks with shapes that vary from angular to rounded; they may also exhibit complex lateral facies variations [Miall, 2014]. The *Aguas de Vichy* thermal springs are probably influenced by multiple water sources, these may include geothermal fluids that rise through convection, meteoric waters, and surface waters from the river and streams that recharge the aquifer. In addition, its dispersion throughout the aquifer may be facilitated by the lateral connectivity and heterogeneity of the alluvial deposit, rather than solely by a saline or geothermal source.

Table 1: Geochemical values corresponding to *Aguas de Vichy* [Alfaro and Ortiz, 2011].

Code	**Location Name**	**Total Alkalinity** (mg CaCO3/L)	**Total Dissolved Solids** (mg/L)	**Na**	**K**	**Mg**	**Ca**	**Mn**	**Fe**
SAN001	Vichy Waters	720	360.2	58.5	20.2	218.5	6	0.08	0.42

The theoretical geothermal reservoir reveals promising potential, according to the estimations done by [Alfaro et al., 2020] using the volumetric model. The estimated reservoir temperature is 100 °C, an ideal temperature that classifies it as a medium-entalphy reservoir. The electrical potential remains at a mean of 80 kWe (0.08 MWe) by Monte Carlo simulation; however, it is important to note that the confidence interval 90% goes from 0.03 to 0.13 MWe, with a standard deviation of 0.04, a median of 0.07 and an uncertainty of 0.04%. The projected life expectancy of the project is 30 years, with an expected recovery factor of 0.10 (Table 2). It is important to note that the volumetric method employed by Alfaro et al. [Alfaro et al., 2020] does not incorporate detailed geological information from the thermal springs under study; rather, it generalizes the reservoir area using computational clusters ranging from 1 km^2 to 3 km^2, assigns standardized reservoir thicknesses from 1 to 2.5 km, and assumes a uniform expected porosity of 0.11 for each thermal spring. Despite the high variability of the estimations and the eventual need for further research, the identified thermal capacity underlines the potential for future development and energy generation.

3 Methods

Geoelectrical methods serve as a practical approach to evaluate convection-dominated geothermal systems and groundwater, as they are sensitive to the presence of fluids. Resistivity measurements, for example, have been extensively utilized in a multitude of geothermal-related studies, such as the one in the Hammam Sayala hot springs [Chabaane et al., 2017], the Langfang geothermal system [Tian et al., 2022], the Krafla geothermal area [Arnason et al., 2000], Los Humeros and Acoluco geothermal systems [Romo-Jones et al., 2021], and the Wairakei-Tauhara field [Hunt et al., 2009]; these applications are discussed in section 1.

Given that temperature and salt concentration have an effect on fluid subsurface conductivity [Hermans et al., 2012, Revil et al., 1998, McInnis et al., 2013] and electric resistivity of soil and rock tend to decrease with temperature [Revil et al., 1998, Llera et al., 1990], thermal saline waters may exhibit lower resistivity in comparison to the Quaternary deposit material and the fresh waters within the aquifer, therefore, Electrical Resistivity Tomography (ERT) is an optimal method for detecting these contrasts and map potential flow paths [Hermans et al., 2012]. This method will assist in the identification of geothermal plumes associated with geothermal fluids and the distinction between them and neutral waters or surrounding materials in the subsurface. Furthermore, we utilized induced polarization (IP) to assess the chargeability of the subsurface materials, thereby enhancing the precision of our subsurface imaging.

We conducted a series of transects over the aquifer, strategically positioned across the inferred fault to track the movement of geothermal plumes and explore their interaction with the fault structure, see Figure 1. Our objective was to test the hypothesis that the fault serves as a primary conduit for the ascent of fluids to the surface. To supplement our data acquisition, we constructed a synthetic model that replicated the subsurface environment. This model consisted of a low-to-medium resistivity aquifer/deposit situated above a fault, which brought into contact the high-resistivity Floresta formation, and the medium-to-high resistivity Tambor formation.

Table 2: Estimated potential in MW - Volumetric model, source: Alfaro et al. (2020).

Stored Heat Parameters			
Parameter	**Minimum**	**Expected**	**Maximum**
Area of the deposit (Km^2)	1.0	2.0	3.0
Thickness of the deposit (Km)	1.0	1.5	2.5
Volume of the deposit (Km^3)	1.0	3.0	7.5
Specific volumetric heat of the rock ($kJ/m^3°C$)	2847	2847	2847
Reservoir temperature (°C)	31	100	100
Reference temperature (°C)	7	13	20
Porosity	0.10	0.11	0.15
Water density (kg/m^3)	958	958	958
Rock density (kg/m^3)	2600	2700	2800
Specific heat of water (kJ/kg K)	4.22	4.22	4.22
Specific heat of the rock (kJ/kg°C)	0.90	1.00	1.10
Electric Potential Parameters			
Recovery factor	0.05	0.10	0.25
Heat recovered from well (KJ)	7.43E+13	7.43E+13	7.43E+13
Project life (Years)	30	30	30
Conversion efficiency	0.00	0.00	0.00
Surface loss factor	0.90	0.90	0.90
Monte Carlo Results			
Stored heat energy (EJ)	Mean: 0.61 90% confidence interval: 0.31 to 0.90 Standard deviation: 0.23		
Electric potential (MWe)	Mean: 0.08 90% confidence interval: 0.03 to 0.13 Standard deviation: 0.04 Median: 0.58 Uncertainty: 0.24%		

3.1 Electrical Resistivity Tomography (ERT) and Induced Polarization (IP)

Electrical Resistivity Tomography (ERT) is a geophysical technique that quantifies the distribution of subsurface resistivity by measuring electrical potentials generated by current injection [Tsourlos, 1995]. This method provides insights into subsurface properties such as fluid contents, porosity, lithologies, and salinity, making it invaluable in mineral, energy exploration, and environmental studies. ERT is grounded in the principle that the subsurface's ability to transmit electrical current varies with its resistivity, an intrinsic property defined by Ohm's law as $V = I \times R$, where V is voltage, I is current, and R is resistance. Resistivity (ρ) is defined as:

$$\rho = R \times \frac{A}{L}$$

Where A is the cross-sectional area through which the current flows, and L is the conductor length. In ERT, this property is crucial as it influences the path and distribution of electrical currents in the

subsurface, dictated by different conduction modes: dielectric, electronic, and electrolytic, the latter being predominant in geological materials due to ion transport in pore fluids.

ERT data acquisition involves the deployment of an array of electrodes in the survey area. Current is injected into the subsurface through a pair of electrodes known as the current electrodes (A and B), and the potential difference is measured between another pair, known as potential electrodes (M and N). The typical setup is to vary the spacing and configuration of these electrodes (e.g., Wenner, Schlumberger, dipole-dipole) to explore different depths and resolve different features:

$$V_{MN} = \frac{\rho I}{2\pi}\left(\frac{1}{r_M} - \frac{1}{r_N}\right)$$

Where V_{MN} is the voltage measured between electrodes M and N, r_M and r_N are the distances from the current source to these electrodes. The apparent resistivity (ρ_a) can then be calculated using the geometric factor (K) of the electrode array:

$$\rho_a = K \times \frac{V_{MN}}{I}$$

Where K is determined by the electrode arrangement and spacing, effectively normalizing the measurements to account for the geometric distribution of the electrodes.

Induced polarization (IP), on the other hand, represents an electrical geophysical technique that employs the capacitive properties of the subsurface to determine the voltage decay over time. This measurement is used to measure the chargeability, which is IP's primary objective. IP involves the injection of current into the ground through two electrodes, with a subsequent measurement of potential across another pair of electrodes after the cessation of current [Dobrin, 1960].

It takes a finite, although short, time before the potential is reached when a current is switched on. Consequently, in sustained current flow, induced polarization manifests as a frequency-dependent impedance variation in the ground. Thus, IP can be observed in the time as well as the frequency domain [Parasnis, 2012]. In time-domain induced polarization, direct current (d.c.) pulses of duration T are introduced into the ground, with observed IP magnitude often expressed as $\Delta V/V$ (millivolt per volt), where ΔV is voltage remaining at a specific time t post current cut-off. This quantification of IP, denoted as P_t^T, corresponds to the material's polarizability. Typical values for T range from 1 to 20 seconds, with t representing a fraction of T. This methodology accentuates voltage decay over time. The ratio $\Delta V/V$ generally remains unaffected by initial voltage V, making it a reliable indicator of the capacitance response of the ground, particularly in scenarios of variable ground properties.

The chargeability $M_{t1,t2}^T$ is often represented as the normalized time integral $(1/V)\int_{t_1}^{t_2} \Delta V dt$, which represents the area under the voltage decay curve. Expressed in millivolt-seconds per volt or miliseconds. This parameter is expressed in millivolt-seconds per volt or miliseconds, and it is significant in delineating materials such as clays, that are known for their electrical charge storage and polarization tendencies. Selecting the appropriate t is key for accurate IP measurements.

The data processing involves steps from raw data acquisition through preprocessing, quality control, and inversion to produce interpretable resistivity models. This process transforms measured voltages and decays into 2D resistivity and chargeability profiles, helping to visualize and quantify subsurface structures and anomalies.

3.2 Synthetic Model

The synthetic model was executed to understand how resistivity inversion would appear under the hypothesized subsurface conditions. PyGIMLi [Rücker et al., 2017], which offers comprehensive

computational tools to simulate complex subsurface resistivities, was employed to this end. Initially, we established a 2D geometric model representing the Floresta formation, the Tambor formation, the aquifer/deposit, and the fault, assigning specific resistivity values to each. The resistivity values were estimated based on the studies of García-Arias et al. [García-Arias et al., 2024] and Saad et al. [Saad et al., 2012]. We set up an electrical resistivity tomography (ERT) measurement scheme using 64 electrodes evenly spaced along a line extending from 0 to 170 units, and used a computational mesh to define the spatial domain. To model the injection of geothermal fluid into the aquifer, an injection point was established at the fault and the intersection of the quaternary deposit. Here, we simulated the geothermal fluid as a diffusive substance with a peak concentration value of 100% at the injection point, applying a diffusion coefficient to represent the spread of the fluid. Boundary conditions included zero concentration (Dirichlet condition) at the external boundary and consistent fluid influx (Neumann condition) at the injection point.

After solving the diffusion equation, we refined the visualization by interpolating the concentration values to the mesh cell centers and reducing any negative concentration values to zero to ensure physical precision. Considering the property of interest is resistivity, a linear inverse relationship between resistivity and concentration of the difussive fluid was established across the aquifer. This relationship ranged from a minimum to a maximum resistivity value, effectively linking concentration with the electrical properties of the geological medium: higher concentrations of the difussive fluid correspond to lower resistivity and vice versa (Figure 2a and 2b).

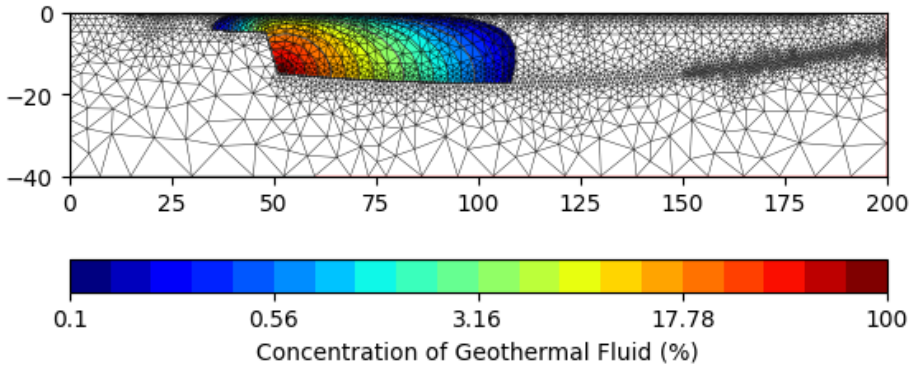

(a)

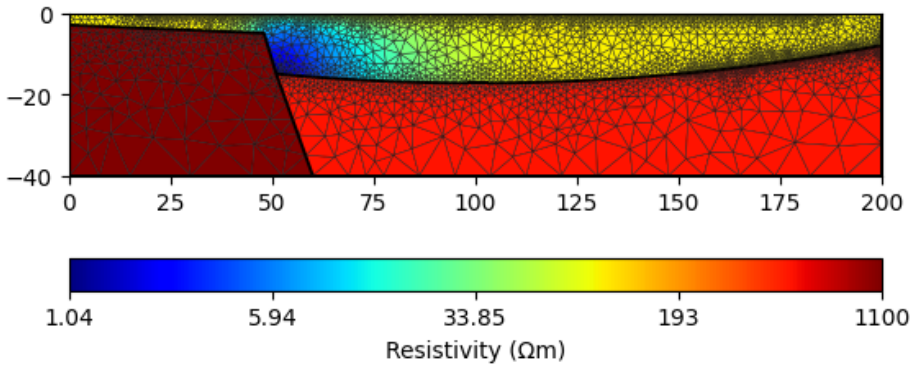

(b)

Figure 2: Overview of the subsurface modeling: (a) Structure of the isolated diffusive fluid (geothermal plume) as a function of its concentration, (b) Synthetic subsurface resistivity including the geothermal plume

Upon completion of the synthetic model, we proceeded to simulate the Electrical Resistivity Tomography (ERT) data, utilizing the calculated resistivity distribution as the model parameter. To achieve the highest level of detail possible, we decided to use the multiple-gradient array for the simulation, because of its proven high resolution and robustness against noise, as substantiated by the findings of [Dahlin and Zhou, 2006]. The efficacy of this array configuration lies in its rapid data acquisition and enhanced data density, essential for intricate subsurface delineation. Moreover, its ability to attenuate noise impacts renders it highly suitable for simulating realistic environmental conditions, thereby bolstering the reliability of the data [Dahlin and Zhou, 2004].

To mirror actual field scenarios, we introduced a noise level of 3% alongside an absolute noise factor of 1×10^{-6}. For consistency and repeatability of the stochastic elements within the model, a fixed random seed (1337) was employed. The inversion of the simulated ERT data was executed using Res2Dinv software [Loke, 2010], and the results, presented in Figure 3, corroborate the detectability of the hypothetical geothermal plume as a discernible low resistivity anomaly. Additionally, these results delineate the fault through a pronounced resistivity gradient and define the aquifer's lower boundary with remarkable clarity.

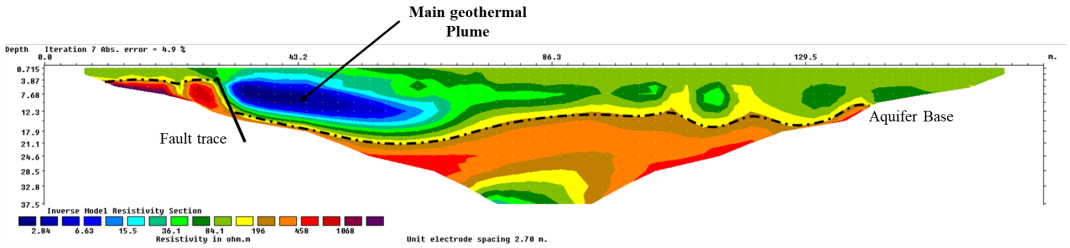

Figure 3: Inverted section of the synthetic model using Res2Dinv, the modelled geothermal plume can be seen as a low resistivity anomaly, while the fault appears as a high gradient of resistivity at the left.

3.3 Data Acquisition and Processing

For the data acquisition, we employed the ZZ-Universal-96 acquisition system manufactured by *ZZ Resistivity Imaging Ltd.* Three Electrical Resistivity Tomography (ERT) transects situated close to the fault map trace were acquired. Two of these transects were complemented with Induced Polarization (IP) measurements, which were employed to enhance the subsurface characterization. Given the nature of the study area's alluvial deposit, which is expected to be characterized by lateral heterogeneities and facies variations [Miall, 2014], a high-detail subsurface image is essential to resolve the deposit's structure.

Since the goal was to achieve sufficient data density, we utilized the proprietary ZZ array of the ZZ Universal 96 acquisition system, which employs full-channel measurements: For every AB current injection, the system measures potential from all other electrodes, significantly increasing the information collected compared to other arrays. This approach ensures enhanced data density and higher resolution, necessary for resolving the subsurface complexity and detecting the expected geothermal plume. It is important to clarify that a minor percentage of the channels presented damage, thereby affecting the measurements. Consequently, it was necessary to remove them from the acquisition. Detailed information on data acquisition is provided in Table 3.

ERT transects 1 and 2 intersected the fault trace near the river on an alluvial terrace (see Figure 1). In contrast, ERT 3 was conducted within the Quaternary deposit and did not intersect the fault, as it was situated farther from both the alluvial terrace and the river course to evaluate the extent of the

geothermal system. The proximity of ERTs 1 and 2 to the river is expected to reveal the phreatic level of the aquifer, which correlates with the topographic elevation of the river trace (Figure 4).

Table 3: Summary of the three ERT surveys, detailing parameters, settings, and geographic coordinates (MAGNA Bogotá). The orientation of all the surveys is SW-NE and the ZZ array was used.

Survey	Name	Channels	Spacing (m)	Length (m)	Unused electrodes	ERT	IP	Start Coordinate	End Coordinate
ERT 1	NOV_24_1	64	3	189	37, 38, 40, 57, 58, 59	Yes	No	1243854.41 N, 1135560.46 E	1244020.64 N, 1135645.85 E
ERT 2	NOV_25_1	64	2.5	157.5	35, 37, 38, 40, 57, 58, 59, 63	Yes	Yes	1242977.403 N, 1135976.464 E	1243131.04 N, 1135988.524 E
ERT 3	NOV_25_2	32	5	155	N/A	Yes	Yes	1244553.70 N, 1135424.43 E	1244708.85 N, 1135453.98 E

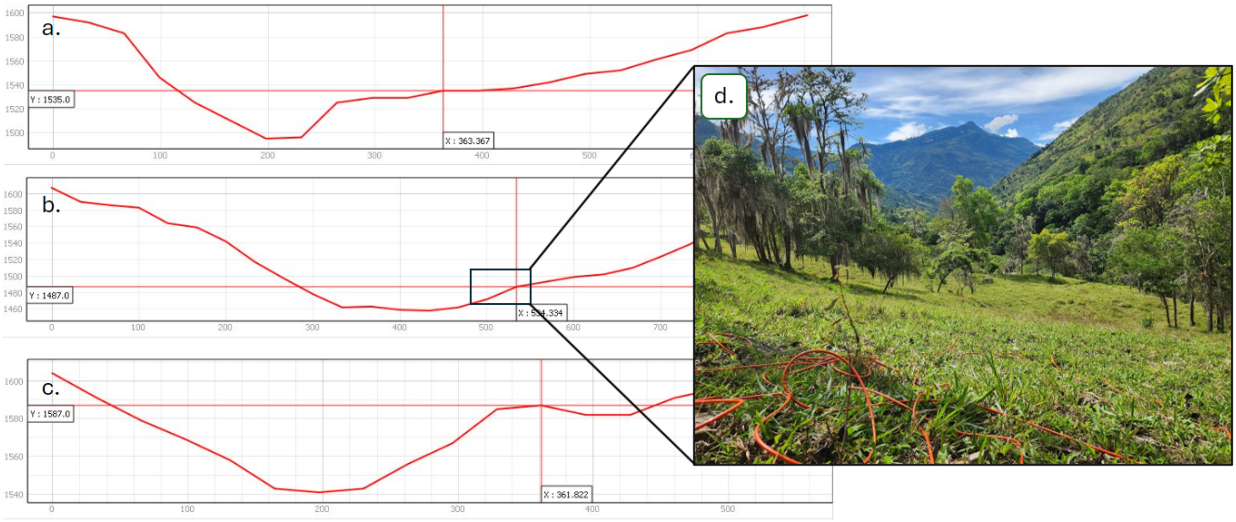

Figure 4: Topographic profiles for the ERT surveys, showing (a) ERT 1, (b) ERT 2, and (c) ERT 3 locations, with an additional (d) detailed view of the ERT 2 study area.

After data acquisition, we initiated the process with a quality control phase to filter unwanted or unreliable data. This involved analyzing the data quality factor (Q), which is a measure used to assess the quality or reliability of data. In Figure 5 it is shown the distribution curve of the electric potential data collected. We established a Q threshold of 30 to selectively filter out data points, according to the manufacturer's recommendation, higher Q values often indicate the presence of various forms of electrical noise, which degrade the quality of the data.

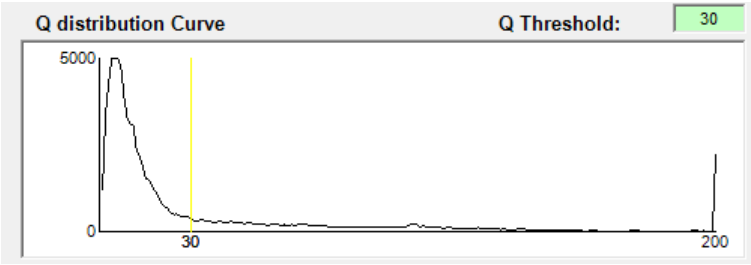

Figure 5: Q distribution curve for the ERT 2.

Subsequently, the data were converted to Res2Dinv [Loke, 2010] format (*.dat*), allowing individual resistivity values to be associated with each AB-MN measurement set. Furthermore, we applied filters to discard any apparent resistivity data below zero and to remove outliers, specifically those values exceeding the 99th percentile, to minimize the impact of extreme resistivity values on the inversion process, ensuring more reliable and accurate subsurface imaging. The topography was added for each electrode as a separate list. For the induced polarization data of ERT 2 and ERT 3 we followed the same workflow to remove outliers and negative values.

The inversion process was performed using Res2Dinv [Loke, 2010]. Inversion parameters have been selected to optimize the accuracy and reliability of the subsurface resistivity characterization. Key parameters chosen include an initial damping factor of 0.15, which helps to stabilize the inversion by controlling the sensitivity of the solution to changes in the model resistivity. This factor was set moderately low to allow for sufficient flexibility in adjusting the model to fit the data without overfitting.

The minimum damping factor was set at 0.03 to ensure that the inversion continues to refine the model even as iterations proceed, preventing stagnation. A particularly important setting is the local optimization option, which allows for localized refinements in the resistivity model, crucial for detecting subtle features and anomalies in heterogeneous subsurface environments. The limit of convergence criteria for relative change in RMS error was set at 2.00 percent and a minimum change in RMS error for line search at 0.50 percent. These settings ensure that the inversion process iterates until a representative model is achieved without excessive computation.

The process involves seven iterations to reach a stable solution without excessive processing time. Additionally, a robust data constraint is applied with a cutoff factor of 0.05, which helps in managing outlier data points that could skew the results. This is complemented by the robust model constraint being deactivated, allowing the model complexity to vary more freely across different subsurface layers. Furthermore, topography is incorporated using a damped Finite Element Method (FEM) setting and an average elevation trend removal.

The extended model configuration was deactivated to restrict the analysis to model cells that correspond directly with collected data points, thereby avoiding extrapolation beyond the actual survey boundaries. This choice is justified by the inherent geological complexity of the subsurface. The high density of the data is critical to detail the complexity of the subsurface resistivity variations. In particular, data points tend to be denser in the upper region of the model blocks arrangement; this data concentration suggests that the resulting resistivity model in this area will be highly detailed and reliable (Figure 6a). In regards to IP, there are fewer chargeability data points and, therefore, a lower data resolution. IP data tend to be denser in the upper region of the arrangement as well (Figure 6b).

After the initial inversion, we analyzed the histogram of the error percentages at all data points. Our focus was on excluding data points where the error exceeded 100%. Concurrently, we examined the scatter plot comparing calculated versus measured apparent resistivity. Our goal was to iteratively remove the most dispersed data points to better align the distribution with the theoretical regression line. This iterative process was applied to both Resistivity and Induced Polarization (IP) measurements until we achieved a satisfactory inversion result with the lowest mean absolute error (MAE) variation. We used the same cell size for both inversions. It is important to note that, despite our efforts, some data points with errors exceeding 100% remained (possibly due to the complexity of the subsurface), but these were substantially minimized (Figure 7).

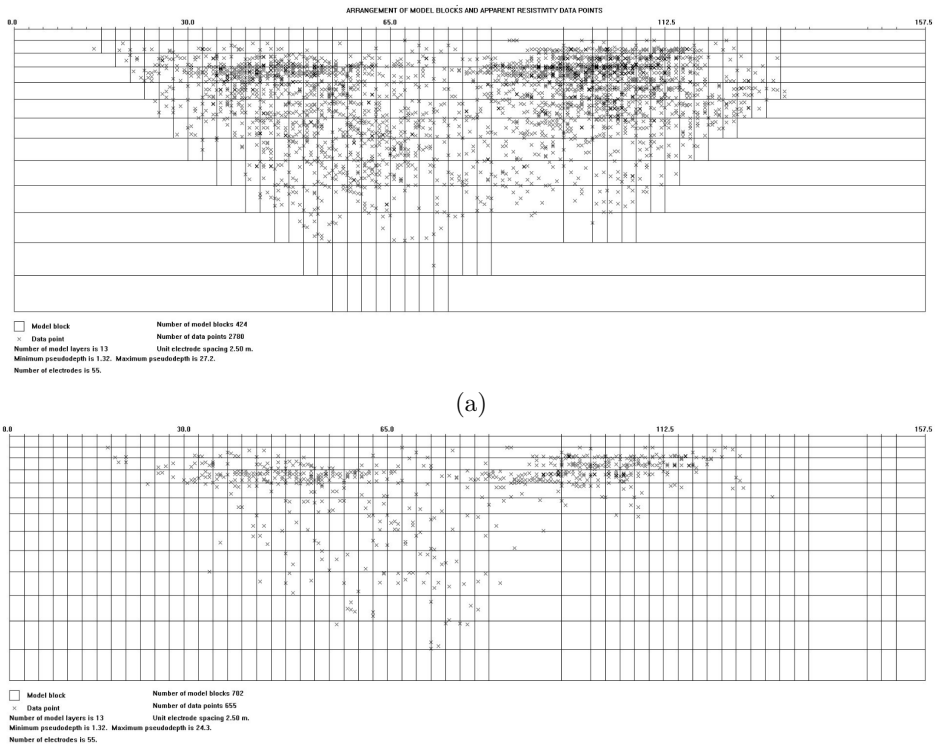

Figure 6: (a) Arrangement of model blocks and distribution of resistivity data points across the ERT 2, (b) Distribution of chargeability data points across the model blocks.

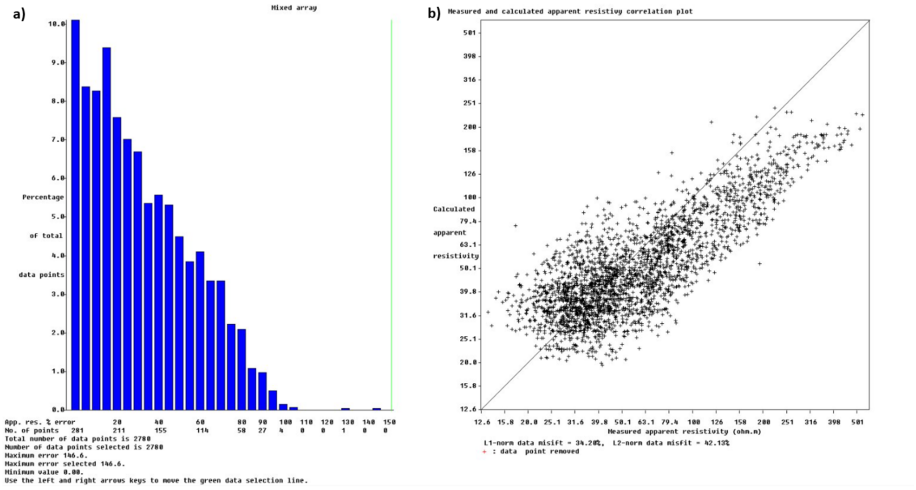

Figure 7: Left: Histogram of error percentages for ERT 2 data, highlighting removal of data points with errors over 100%. Right: Scatter plot of calculated vs. measured apparent resistivity, showing the alignment of data around the theoretical line post-cleanup.

4 Results and Discussion

ERT and IP surveys were conducted on the aquifer associated with the *Aguas de Vichy* thermal springs, through this process, we successfully generated five geoelectrical profiles of the subsurface,

comprising three resistivity profiles and two chargeability profiles. Our results provide information on the physical properties of the subsurface. This allowed us to confirm the presence of the previously inferred fault, detect thermal water plumes associated with the fault and the base of the aquifer. To ensure visual consistency when comparing the results of the three ERT surveys, we standardized the color scale across all surveys using the same color scale. Specifically, the lower limit of the color scale was set to match the lowest resistivity value observed among the three surveys. The interpretation of our results is based on direct and indirect measurements of subsurface materials from different authors (Table 4).

Table 4: Resistivity and Chargeability values for different materials.

Material	**Resistivity (ohm.m)**	**Chargeability (msec)**	**References**
Groundwater	10 - 150	< 1	[Telford et al., 1990], [Murali and Patangay, 2006], [Akhtar et al., 2021]
Hot saline water plume	0.2 - 5	< 1	[Chabaane et al., 2017], [Hermans et al., 2012]
Clay	5 - 160	15-90	[McCarter, 1984], [Sill and Klein, 1981], [Suryadi et al., 2019]
Sand	40 - 1500	2-12	[Telford et al., 1990], [Abd Malik et al., 2022], [Murali and Patangay, 2006]
Alluvium	10 - 800	1 - 4	[Telford et al., 1990], [Murali and Patangay, 2006]
Sandstone	8 - 4 x 10^3	3 - 12	[Telford et al., 1990], [Abd Malik et al., 2022], [Murali and Patangay, 2006]

The ERT 1 resistivity profile (Figure 8) displays resistivity values ranging from 2.82 Ω.m to over 2000 Ω.m, with lower resistivities corresponding to thermal water and mixed thermal and fresh water. It's important to note that this profile features a pronounced thermal water plume on its southwestern side, sharply delineated by a resistivity gradient that can be interpreted as a fault. This association suggests that the fault serves as a primary conduit for the thermal fluids to infiltrate into the aquifer via convection, driven by density and temperature differences [Zongjun et al., 2014].

The resistivity profile also shows similarity to the synthetic model shown in Figure 3, particularly in identifying the geothermal plume and the fault. However, the resulting section from ERT 1 is more complex, supporting our initial thoughts about the subsurface heterogeneity associated to the alluvial deposit, characterized by facies variations, see [Miall, 2014]. This alluvial deposit has also been classified as consisting predominantly of intercalations of sand, gravel, and clay [Ríos et al., 2002]. This heterogeneity results in zones of both high and low permeability, affecting the dispersion and diffusion of the thermal plume. Such fluvial depositional environments lead to an irregular pattern of thermal water distribution, contrasting with the uniform distribution observed in the synthetic model. There is an interesting high resistivity anomaly right above the main geothermal plume, which may correspond to low-permeability sandy facies, and are likely affecting the resistivity representation of the main plume in the inverted section.

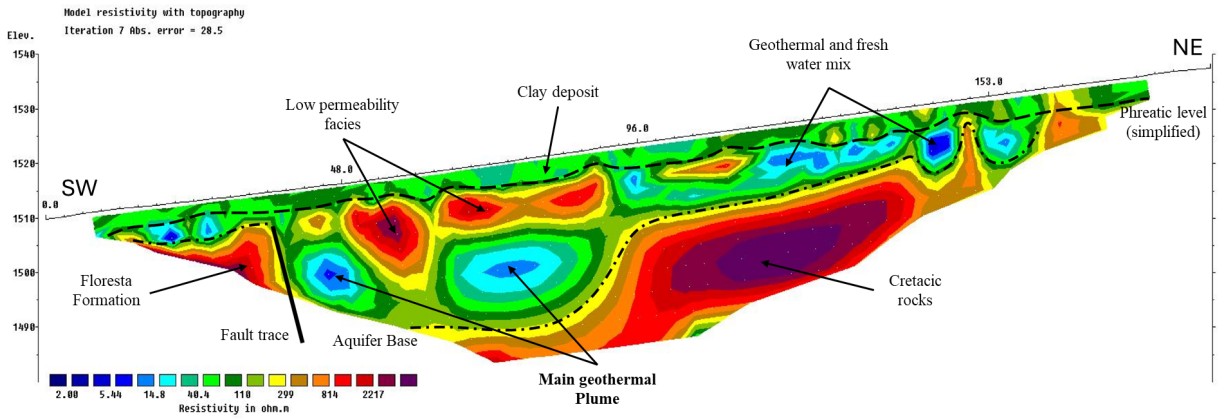

Figure 8: Inverted resistivity profile for ERT 1, highlighting the fault trace, the main geothermal plume, the aquifer base, and the lateral heterogeneity of the subsurface.

The phreatic level of the aquifer is inferred to be situated just above the majority of the low-resistivity zones associated with thermal water. This level aligns with the topographic elevation of the Guaca River, which is slightly above 1500 meters above sea level (MASL), as illustrated in Figure 4a. It is important to mention that the phreatic level may be more complex and irregular due to the complexity of the subsurface; however, we have provided a simplified representation. Above this phreatic level, zones of low to moderate resistivity are observed, suggesting the presence of a clay layer that may locally confine the aquifer, this clay layer may be laterally discontinuous as there are resistivity variations. The base of the aquifer, as well as the underlying Cretaceous rocks and the Floresta Formation, are also discernible in the resistivity profile.

Given that low resistivity anomalies are consistently distributed throughout the resistivity profile, it can be suggested that the aquifer, despite its lateral facies variations, has significant continuity. This continuity facilitates the movement of geothermal fluid through it, which supports the previous hypothesis that the thermal waters occur due to an advective flow withing the aquifer [Alfaro, 2017] towards the thermal springs. The identified thermal plume suggest that the geothermal fluid not only moves laterally, but it ascend through the main fault due to heating in deep and convection.

The inverted resistivity section of ERT 2 (Figure 9a) reveals subsurface features consistent with those observed in ERT 1. The resistivity profile displays irregularly distributed, prominent low-resistivity zones throughout the aquifer, indicative of the presence of geothermal fluids, fresh water mix, and saturated clays. These zones are flanked by areas of higher resistivity, likely representing more consolidated or less saturated materials, which emphasize the lateral facies variations characteristic of the aquifer. The profile also delineates a pronounced resistivity gradient towards the northeast (right side of the section), marking the fault trace. Adjacent to this fault, the main geothermal plume is visible, suggesting the fault's role as a primary conduit for thermal waters infiltrating the aquifer. Both the phreatic level and the aquifer base are visible within the section, alongside the Floresta Formation situated beneath the aquifer. A discontinuous clay layer at the top is also identified, potentially acting to locally confine the aquifer and, therefore, limiting its recharge through meteoric waters.

Additionally, the IP profile done in the same transect of ERT 2 (Figure 9b), although offering less coverage deeper in the section and displaying most data points near the surface (as illustrated in Figure 6b), complements the resistivity data. It highlights regions of both low and high chargeability. The high chargeability at the top of the IP section is associated with polarizable materials such as clay,

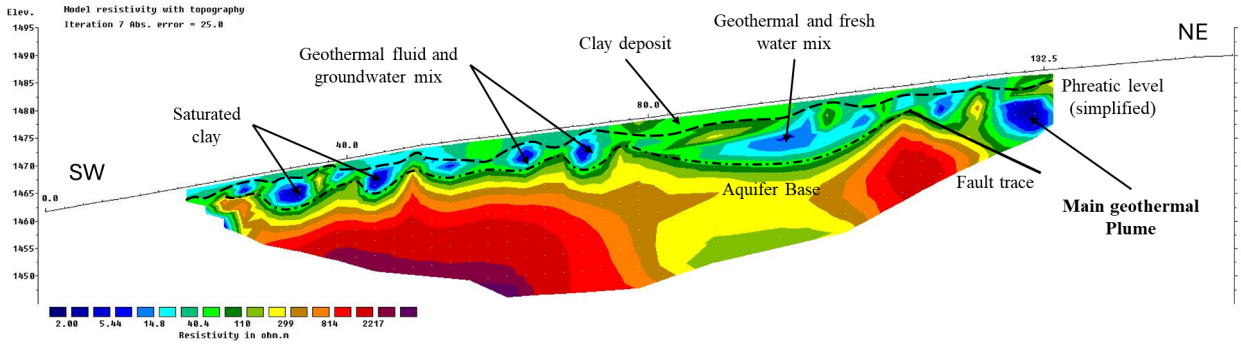

(a)

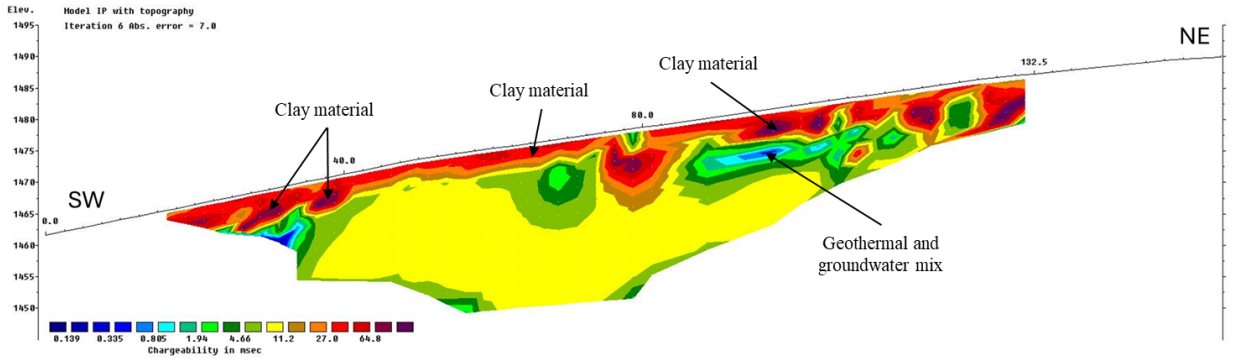

(b)

Figure 9: Inverted ERT 2 profiles, showing resistivity (a) and IP data (b). Key features include saturated clays, a clay layer, the main fault trace and the main geothermal plume identified.

supporting the identification of this material within the deposit. Meanwhile, the low chargeability zones may validate the presence of geothermal fluids as they seem to be correlated with conductive zones, although less distinct than in the resistivity profile due to having fewer data and different resolution.

The geophysical signatures observed in ERT 1 and ERT 2 sections support the idea that thermal waters are rising along the fault and spreading laterally within the aquifer, influenced by the complex interplay of geological facies and fluid dynamics. This dynamic not only suggests the presence of geothermal activity within the aquifer but also provides insights into the origin of the *Aguas de Vichy* thermal springs. The complex interaction between the convective flow of thermal waters through the fault and their dispersion through heterogeneous, permeable media enhances our understanding of the geothermal system and the aquifer's hydrogeological behavior

The inverted section of ERT 3 (Figure 10) differs significantly from the previous surveys by not crossing the fault and being located topographically further from the river compared to ERT 1 and ERT 2. This section predominantly displays patterns consistent with a clay deposit rather than signs of geothermal activity. The resistivity profile (Figure 10a) exhibits higher resistivity values which might indicate less saturated zones, while localized lower resistivity areas suggest pockets of higher saturation or slightly different material composition, likely still within the predominantly clay deposit.

The IP profile (Figure 10b) supports this interpretation by mostly showing areas of higher chargeability, which are typical for clay-rich formations due to their ability to polarize under an electrical field. The absence of significant geothermal signatures and the relative consistency across the section suggest

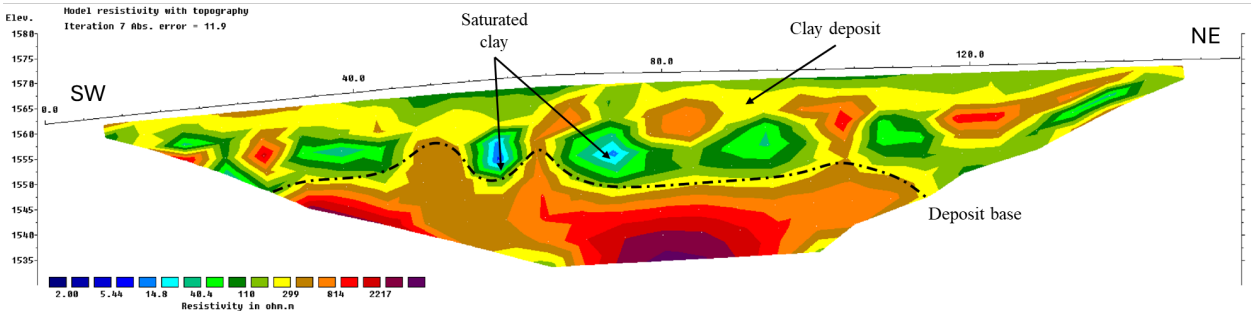

(a)

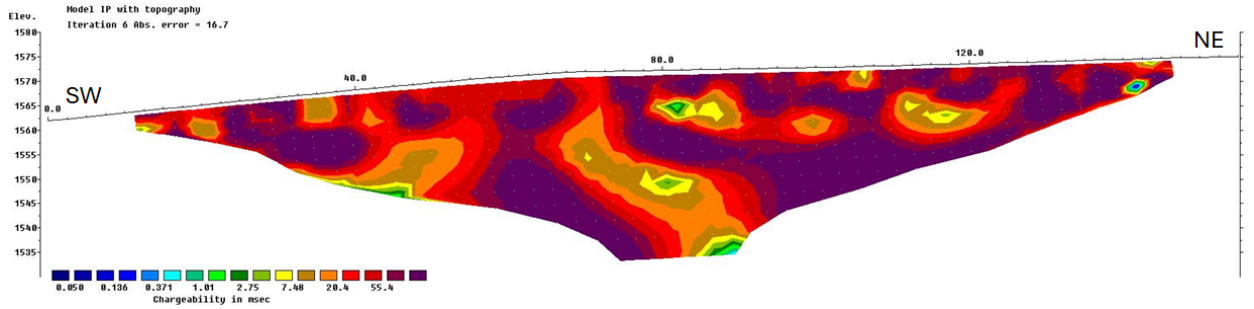

(b)

Figure 10: Inverted ERT 3 resistivity (a) and IP (b) profiles displaying subsurface features in the *Aguas de Vichy* area. Key elements include saturated clay layers and clay deposits, with a clear delineation of the deposit base.

that this area of the deposit does not contribute to the geothermal dynamics and the fluid circulation observed in other sections. Instead, it likely represents a more isolated or confined portion of the depositional system which is not as related to the river as the other two profiles, and its characterized by its clay content which may act as a barrier or confining layer within the hydrogeological context. The results of the ERT 3 support the essential role of faulting in channeling and concentrating geothermal fluid in the aquifer, and therefore, the possibility of a convective domain.

Despite the limited scope of detailed studies in the region, previous research by [Alfaro et al., 2020] has demonstrated substantial geothermal potential. The volumetric method and Monte Carlo simulations suggest a promising outlook for geothermal energy development, with expected electric potential capable of meeting regional energy demands (Table 2). Despite the promising geothermal potential and a viable reservoir temperature of 100°C, further exploration and detailed studies are necessary to more accurately assess the geothermal capabilities of the *Aguas de Vichy* springs, as the potential estimated for the thermal springs relies on standardized and generalized parameters rather than specific properties of the geothermal reservoir.

Future work should aim to locate the heat source responsible for the thermal characteristics of the waters, exploring deeper geological structures that could be influencing the thermal regime. Further detailed geophysical surveys, potentially including deeper seismic profiling and gravimetric or magnetotelluric studies, could provide critical data to guide the exploration of boreholes, geothermal gradient wells and further surface temperature measurements. Gamma-spectrometer measurements can offer valuable insights into the water's radioactivity and its potential heating through radioactive decay, and laboratory measurements of geoelectrical properties on rock samples from boreholes or outcrops can also be beneficial. These efforts would not only advance our geological understanding

but could also lay the groundwork for sustainable geothermal development, contributing to regional energy security. Additionally, this research supports the potential establishment of health and wellness centers that leverage the unique thermal properties of the *Aguas de Vichy* springs, which could foster new opportunities for regional development through tourism.

Conclusion

The integration of high-resolution geophysical methods, specifically Electrical Resistivity Tomography (ERT) and Induced Polarization (IP), has significantly advanced our understanding of the subsurface structure at the *Aguas de Vichy* thermal springs. ERT data was used to define the origin and distribution of the geothermal plume within the aquifer, showing that the geothermal fluid is housed in a laterally-varying aquifer with sand, clay and conglomerates; such facies variations are in agreement with the expected subsurface complexity due to the fluvial depositional system. IP data were useful to identify the clay levels that locally confine the aquifer.

Our research indicates the existence of a complex geothermal system, closely interlinked with the region's geological and structural attributes, especially fault systems that facilitate the movement and convection of geothermal fluids. The results of our study support the hypothesis that the *Aguas de Vichy* springs are influenced by deep infiltration from a saline source [Alfaro and Ortiz, 2011], with their emergence at the surface driven by advective flow within the aquifer. Nonetheless, the detection of a geothermal plume associated with the fault trace suggests an upward migration of thermal waters into the aquifer, possibly due to a deep-seated heat source, suggesting a convection-dominated geothermal system rather than being solely advection-dominated as initially proposed by [Alfaro, 2017].

Finally, this study underscores the necessity for ongoing exploration and in-depth analysis of the *Aguas de Vichy* geothermal system, as well as other potential sites in Santander and across Colombia. Such efforts will be significant for the effective integration of geothermal energy into the nation's broader energy strategy, facilitating Colombia's transition towards a more sustainable and diversified energy future.

References

[Abd Malik et al., 2022] Abd Malik, A. K., Madun, A., Dan, M. F. M., Tajudin, S. A. A., Talib, M. K. A., Azmi, M. I. S., Noh, K. A. M., and Joret, A. (2022). The effect of particle size towards resistivity and chargeability for groundwater interpretation. In *IOP Conference Series: Earth and Environmental Science*, volume 1003, page 012031. IOP Publishing.

[Akhtar et al., 2021] Akhtar, N., Mislan, M., Syakir, M., Anees, M. T., and Yusuff, M. (2021). Characterization of aquifer system using electrical resistivity tomography (ert) and induced polarisation (ip) techniques. In *IOP Conference Series: Earth and Environmental Science*, volume 880, page 012025. IOP Publishing.

[Alfaro, 2017] Alfaro, C. (2017). Geotermia en colombia: Proyecciones y plan de trabajo del servicio geológico colombiano. In *Reunion Nacional de Geotermia*, Manizales, Colombia. Servicio Geológico Colombiano. Coordinadora Grupo Investigación y Exploración de Recursos Geotérmicos.

[Alfaro and Ortiz, 2011] Alfaro, C. M. and Ortiz, I. D. (2011). Inventario nacional de manantiales termales fase 2010, departamento de boyaca, santander y norte de santander. Technical report, Instituto Colombiano de Geología y Minería (INGEOMINAS).

[Alfaro et al., 2020] Alfaro, C. M., Rueda Gutiérrez, J. B., Casallas, Y. P., Rodríguez, G. Z., and Malo, J. E. (2020). Estimación preliminar del potencial geotérmico de colombia. Technical report, Servicio Geológico Colombiano, Bogotá.

[Arnason et al., 2000] Arnason, K., Karlsdottir, R., Eysteinsson, H., Flóvenz, Ó., and Gudlaugsson, S. T. (2000). The resistivity structure of high-temperature geothermal systems in Iceland. In *Proceedings of the World Geothermal Congress 2000, Kyushu-Tohoku, Japan*, pages 923–928.

[Bona and Coviello, 2016] Bona, P. and Coviello, M. F. (2016). Valoración y gobernanza de los proyectos geotérmicos en américa del sur: una propuesta metodológica.

[Bu et al., 2012] Bu, X., Ma, W., and Li, H. (2012). Geothermal energy production utilizing abandoned oil and gas wells. *Renewable Energy*, 41:80–85.

[Chabaane et al., 2017] Chabaane, A., Redhaounia, B., and Gabtni, H. (2017). Combined application of vertical electrical sounding and 2d electrical resistivity imaging for geothermal groundwater characterization: Hammam sayala hot spring case study (nw tunisia). *Journal of African Earth Sciences*, 134:292–298.

[Chandrasekharam and Bundschuh, 2008] Chandrasekharam, D. and Bundschuh, J. (2008). *Low-enthalpy geothermal resources for power generation*. CRC press.

[Dahlin and Zhou, 2004] Dahlin, T. and Zhou, B. (2004). A numerical comparison of 2d resistivity imaging with 10 electrode arrays. *Geophysical prospecting*, 52(5):379–398.

[Dahlin and Zhou, 2006] Dahlin, T. and Zhou, B. (2006). Multiple-gradient array measurements for multichannel 2d resistivity imaging. *Near Surface Geophysics*, 4(2):113–123.

[Dentith and Mudge, 2014] Dentith, M. and Mudge, S. T. (2014). *Geophysics for the mineral exploration geoscientist*. Cambridge University Press.

[Dobrin, 1960] Dobrin, M. B. (1960). *Introduction to Geophysical Prospecting*. McGraw-Hill Book Company Inc., New York, NY.

[García-Arias et al., 2024] García-Arias, S., Patiño, F. A. V., Gómez, J. D. S., and Ardila, M. T. U. (2024). Mapas predictivos con redes neuronales a partir de propiedades físicas de las rocas: caso de estudio en la mesa de los santos (santander). *Revista EIA*, 21(41):4112–pp.

[Gawell et al., 1999] Gawell, K., Reed, M., and M., W. (1999). *Preliminary Report: Geothermal Energy, the Potential for Clean Power from the Earth*. Geothermal Energy Association Report.

[González-Idárraga, 2020] González-Idárraga, C. E. (2020). Caracterización resistiva 3d del área geotérmica de paipa, colombia. *Boletín de Geología*, 42(3):81–97.

[Hermans et al., 2012] Hermans, T., Vandenbohede, A., Lebbe, L., and Nguyen, F. (2012). A shallow geothermal experiment in a sandy aquifer monitored using electric resistivity tomography. geophysics 77: B11–b21.

[Hunt et al., 2009] Hunt, T. M., Bromley, C. J., Risk, G. F., Sherburn, S., and Soengkono, S. (2009). Geophysical investigations of the wairakei field. *Geothermics*, 38(1):85–97.

[(IGA), 2014] (IGA), I. G. A. (2014). *Best Practices Guide for Geothermal Exploration*. IGA Service GmbH, Bochum Germany.

[Jorquera, 2021] Jorquera, C. (2021). Inaugurada primera planta de energía geotérmica en colombia. Retrieved from `https://www.piensageotermia.com/inaugurada-primera-planta-de-energia-geotermica-en-colombia/`.

[Kana et al., 2015] Kana, J. D., Djongyang, N., Raïdandi, D., Nouck, P. N., and Dadjé, A. (2015). A review of geophysical methods for geothermal exploration. *Renewable and Sustainable Energy Reviews*, 44:87–95.

[Llera et al., 1990] Llera, F. J., Sato, M., Nakatsuka, K., and Yokoyama, H. (1990). Temperature dependence of the electrical resistivity of water-saturated rocks. *Geophysics*, 55(5):576–585.

[Loke, 2010] Loke, M. H. (2010). Res2dinv ver. 3.59 for windows xp/vista/7.

[López-Ramos et al., 2022] López-Ramos, E., Gonzalez-Penagos, F., Patiño, C. A., and López, A. (2022). Low-medium enthalpy geothermal resource assessment in deep reservoirs of the llanos basin-colombia. *CT&F-Ciencia, Tecnología y Futuro*, 12(1):13–44.

[McCarter, 1984] McCarter, W. (1984). The electrical resistivity characteristics of compacted clays. *Geotechnique*, 34(2):263–267.

[McInnis et al., 2013] McInnis, D., Silliman, S., Boukari, M., Yalo, N., Orou-Pete, S., Fertenbaugh, C., Sarre, K., and Fayomi, H. (2013). Combined application of electrical resistivity and shallow groundwater sampling to assess salinity in a shallow coastal aquifer in benin, west africa. *Journal of hydrology*, 505:335–345.

[Mejía et al., 2014] Mejía, E., Rayo, L., Méndez, J., and Echeverri, J. (2014). Geothermal development in colombia. *Short Course VI on Utilization of Low-and Medium-Enthalpy Geothermal Resources and Financial Aspects of Utilization*, pages 1–7.

[Miall, 2014] Miall, A. D. (2014). *Fluvial depositional systems*, volume 14. Springer International Publishing, Cham.

[Morales et al., 2021] Morales, E., Veroslavsky, G., Manganelli, A., Marmisolle, J., Pedro, A., Samaniego, L., Plenc, F., Umpiérrez, R., Ferreiro, M., and Morales, M. (2021). Potential of geothermal energy in the onshore sedimentary basins of uruguay. *Geothermics*, 95:102165.

[Murali and Patangay, 2006] Murali, S. and Patangay, N. (2006). Principles of application of groundwater geophysics. *Association of Geophysicists, Hyderabad, India*, 371.

[Márquez et al., 2021] Márquez, I. D., Puyo, D. M., Robledo, M. L., and Valderrama, S. S. (2021). Transición energética: un legado para el presente y el futuro de colombia.

[Ovalle, 2020] Ovalle, J. A. (2020). Geotermia en la región central. convenio interadministrativo 080 de 2019. Región Administrativa y de Planeación Especial RAP-E - Universidad Distrital Francisco José de Caldas.

[Parasnis, 2012] Parasnis, D. S. (2012). *Principles of applied geophysics*. Springer Science & Business Media.

[Pesce and Miranda, 2003] Pesce, A. and Miranda, F. (2003). *Catálogo de manifestaciones termales de la República Argentina. Vol. I-II Región Noroeste*. SEGEMAR, Buenos Aires.

[Revil et al., 1998] Revil, A., Cathles Iii, L., Losh, S., and Nunn, J. (1998). Electrical conductivity in shaly sands with geophysical applications. *Journal of Geophysical Research: Solid Earth*, 103(B10):23925–23936.

[Romo-Jones et al., 2021] Romo-Jones, J. M., Arango-Galván, C., Ruiz-Aguilar, D., Avilés-Esquivel, T., and Salas-Corrales, J. L. (2021). 3d electrical resistivity distribution in los humeros and acoculco geothermal zones, mexico. *First EAGE Workshop on Geothermal Energy in Latin America*, 2021(1):1–5.

[Ríos et al., 2002] Ríos, M., Hincapié, G., and Cardona, A. (2002). Atlas de aguas subterráneas de colombia (versión 2.0).

[Rücker et al., 2017] Rücker, C., Günther, T., and Wagner, F. (2017). pygimli: An open-source library for modelling and inversion in geophysics. *Computers and Geosciences*, 109:106–123.

[Saad et al., 2012] Saad, R., Nawawi, M. N. M., and Mohamad, E. T. (2012). Groundwater detection in alluvium using 2-d electrical resistivity tomography (ert). *Electronic Journal of Geotechnical Engineering*, 17:369–376.

[Salazar et al., 2017] Salazar, S. S., Muñoz, Y., and Ospino, A. (2017). Analysis of geothermal energy as an alternative source for electricity in colombia. *Geothermal Energy*, 5(1):1–12.

[Sill and Klein, 1981] Sill, W. and Klein, J. D. (1981). The electrical properties of clay. Technical report, United States Geological Survey.

[Spichak and Manzella, 2009] Spichak, V. and Manzella, A. (2009). Electromagnetic sounding of geothermal zones. *Journal of Applied Geophysics*, 68(4):459–478.

[Suryadi et al., 2019] Suryadi, A., Amir, S., et al. (2019). Electrical resistivity imaging (eri) and induced polarization (ip) survey to solve water drought problem at alor gajah, melaka, malaysia. In *IOP Conference Series: Materials Science and Engineering*, volume 532, page 012025. IOP Publishing.

[Telford et al., 1990] Telford, W. M., Geldart, L. P., and Sheriff, R. E. (1990). *Applied geophysics*. Cambridge university press.

[Tian et al., 2022] Tian, B., Lei, X., Jiang, H., Xu, C., and Song, M. (2022). Multi-method geophysical mapping of a geothermal reservoir and buried channel in langfang, northern part of china. *Journal of Environmental and Engineering Geophysics*, 27(1):1–11.

[Tsourlos, 1995] Tsourlos, P. (1995). *Modelling, interpretation and inversion of multielectrode resistivity survey data*. PhD thesis, University of York.

[Ward et al., 1977] Ward, D., Goldsmith, R., Survey., U. G., Cruz, J., Jaramillo, L., and Vargas, R. (1977). *Geología de la Plancha 121 Cerrito. Escala 1:100.000*. Ingeominas.

[Zohdy et al., 1974] Zohdy, A. A., Eaton, G. P., and Mabey, D. R. (1974). Application of surface geophysics to ground-water investigations.

[Zongjun et al., 2014] Zongjun, G., Yonggui, L., and Yaun, G. (2014). The principle of density differences drive geothermal water to move and the short-range recharge model of geothermal water in hilly area. In *Proceedings of the Thirty-Ninth Workshop on Geothermal Reservoir Engineering PROCEEDINGS, Stanford, CA, USA*, pages 24–26.